Article

Crystal and Substituent Effects on Paramagnetic NMR Shifts in Transition-Metal Complexes

Jan Novotný,[∇] Lukáš Jeremias,[∇] Patrick Nimax, Stanislav Komorovsky, Ivo Heinmaa, and Radek Marek*

Read Online

ACCESS | Metrics & More | Article Recommendations | SI Supporting Information

ABSTRACT: Nuclear magnetic resonance (NMR) spectroscopy of paramagnetic molecules provides detailed information about their molecular and electron-spin structure. The paramagnetic NMR spectrum is a very rich source of information about the hyperfine interaction between the atomic nuclei and the unpaired electron density. The Fermi-contact contribution to ligand hyperfine NMR shifts is particularly informative about the nature of the metal–ligand bonding and the structural arrangements of the ligands coordinated to the metal center. In this account, we provide a detailed experimental and theoretical NMR study of compounds of Cr(III) and Cu(II) coordinated with substituted acetylacetonate (acac) ligands in the solid state. For the first time, we report the experimental observation of extremely paramagnetically deshielded ^{13}C NMR resonances for these compounds in the range of 900−1200 ppm. We demonstrate an excellent agreement between the experimental NMR shifts and those calculated using relativistic density-functional theory. Crystal packing is shown to significantly influence the NMR shifts in the solid state, as demonstrated by theoretical calculations of various supramolecular clusters. The resonances are assigned to individual atoms in octahedral Cr(acac)$_3$ and square-planar Cu(acac)$_2$ compounds and interpreted by different electron configurations and magnetizations at the central metal atoms resulting in different spin delocalizations and polarizations of the ligand atoms. Further, effects of substituents on the ^{13}C NMR resonance of the ipso carbon atom reaching almost 700 ppm for Cr(acac)$_3$ compounds are interpreted based on the analysis of Fermi-contact hyperfine contributions.
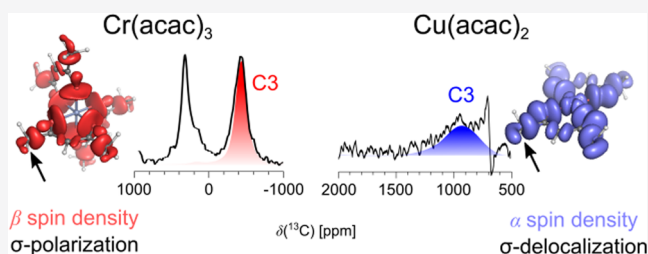
1. INTRODUCTION

Nuclear magnetic resonance (NMR) spectroscopy of para-magnetic molecules[1,2] has been shown to be an excellent technique for investigating the distribution of spin density[3] and the metal–ligand bonding[4] in open-shell systems. The resonance frequencies of paramagnetic species typically lie outside the normal range of NMR shifts for their diamagnetic analogs as a result of the additional contribution of hyperfine (de)shielding, which originates in the hyperfine interaction between the nuclear magnetic moment of a ligand atom L and unpaired electron(s). Because the magnetization of unpaired electron(s) is temperature dependent, its transcription to the hyperfine (HF) NMR shift, δ_L^{HF}, is also temperature dependent. Therefore, measurements at various temperatures are frequently used to estimate the temperature-dependent contribution to the NMR shift and to determine the distribution of spin density.[1,2] However, to interpret the experimental NMR observations in detail, theoretical analysis based on first-principles calculations is typically required.[5] The total NMR shift of atom L can be calculated as the sum of the orbital (δ_L^{orb}, approximately temperature independent) and hyperfine (δ_L^{HF}, temperature dependent) contributions[6,7]

$$\delta_L^{tot} = \delta_L^{orb} + \delta_L^{HF} \tag{1}$$

The hyperfine NMR shift can be related directly to the parameters of the EPR spin Hamiltonian, as shown for doublet systems by Moon and Patchkovskii[6] and later extended to systems with an arbitrary spin degeneracy by Van den Heuvel and Soncini[8,9] and others.[10−15] In the case of vanishing or negligible zero-field splitting (ZFS), and when the degenerate ground state with $2S + 1$ multiplicity is well separated from any excited states, the temperature-dependent part of the isotropic NMR shift obeys the Curie law and is calculated as

$$\delta_L^{HF} = \frac{S(S + 1)}{3} \frac{\mu_e}{3kT\hbar\gamma_L} Tr[\mathbf{g}\,\mathbf{A}^T(L)] \tag{2}$$

Here, we have adopted SI units, kT represents the thermal energy, $\hbar$ is the reduced Planck constant, μ_e is the Bohr magneton, γ_L is the gyromagnetic ratio of nucleus L, and the EPR parameters $\mathbf{g}$ and $\mathbf{A}$ are the $\mathbf{g}$-tensor and the hyperfine coupling tensor ($\mathbf{A}$-tensor), respectively.
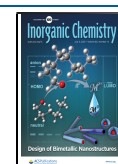
Using the EPR parameters, the δ_L^{HF} can be separated into the Fermi-contact (FC),[5,16] spin-dipolar (SD),[16,17] and paramagnetic spin−orbit (PSO)[16,18] terms used in eq 3, which is governed by the physical terms of the **A**-tensor.[16]

$$\delta_L^{HF} = \delta_L^{FC} + \delta_L^{SD} + \delta_L^{PSO} \qquad (3)$$

The Fermi-contact term, δ_L^{FC}, can be linked directly to the spin density at the position of the nucleus L being probed and will be shown to be dominant for the ^{13}C NMR shifts of the ligand atoms of Cr(III) and Cu(II) compounds **1a−1d** and **2a−2d** (for structures, see Figure 1) investigated in this work.
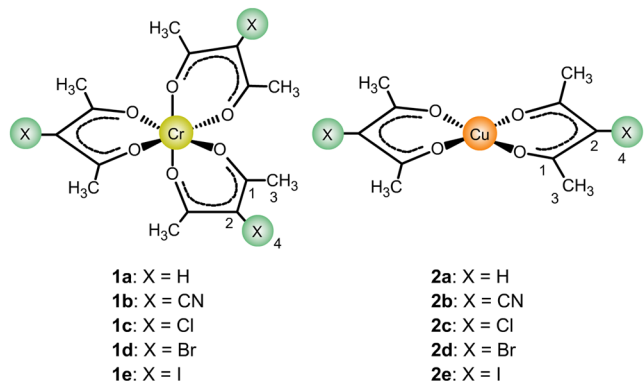
Figure 1. Structures and atom numbering schemes for compounds **1a−1e** (chromium) and **2a−2e** (copper).

We recently provided a clear theoretical interpretation of the signs of the electronic g-shifts and hyperfine coupling constants of eq 2 for iridium complexes with a straightforward generalization covering the full d-block.[18] Early transition-metal (TM) complexes with low d-electron occupancy (d^1–d^3) exhibit negative g-shifts, whereas late transition-metal complexes (d^7–d^9) typically have positive g-shifts. The sign of the isotropic g-shift for the Cr(III) and Cu(II) compounds being investigated (Figure 1) can also be described by a linear spin−orbit approach to the **g**-tensor in the framework of crystal-field theory.[19,20] Recently, the relationship between the electron configuration and the sign of the hyperfine NMR shifts of the ligand has been demonstrated for a series of acetylacetonato vanadium, nickel, and copper complexes.[21] Previous EPR and paramagnetic NMR studies of transition-metal complexes of acetylacetonate include those of Cr(III),[22,23] Mn(III),[23] Fe(III),[22,23] Ru(III),[22−24] Ni(II),[25,26] and Cu(II)[23] compounds.

In this study, we focus on representatives of early (chromium, group 6) and late (copper, group 11) 3d transition-metal compounds with various substituents, as shown in Figure 1. Their previous characterizations by NMR spectroscopy relied mostly on ^{1}H NMR experiments, with ^{13}C NMR data, in most cases, missing or incomplete. Here, we report a full set of ^{1}H and ^{13}C NMR shifts for the parental compounds **1a** and **2a** determined experimentally in the solid state using magic-angle spinning (MAS) experiments with a short echo delay. In addition, relativistic density-functional theory (DFT) calculations[27] were performed to assist in assigning the resonances and to interpret the spin distribution in these compounds along with the Fermi-contact contributions to the hyperfine NMR shifts that are related to it.

2. RESULTS AND DISCUSSION

2.1. Solid-State ^{13}C NMR Shifts. The Cr(III) and Cu(II) compounds were prepared as summarized in the Supporting Information. Their NMR spectra were recorded in the solid state under magic-angle spinning (MAS) at 30 kHz. The ^{13}C MAS NMR spectra of parent compounds **1a** and **2a** recorded at 313 K are shown in Figure 2 as examples.

In contrast to previous reports, we succeeded in measuring all of the ^{13}C NMR resonances[22] of compound **1a** and a very broad resonance[21] at around 900 ppm of **2a**. The measured ^{1}H (solution) and ^{13}C (solid state) NMR shifts for compounds **1a−d** and **2a−d** are summarized in Table 1.

The ^{13}C NMR shifts clearly indicate the different electron configurations and spin distributions in the groups of compounds **1** and **2**. In compound **1a**, the carbonyl atom C1 is greatly paramagnetically deshielded ($\delta = +1155$ ppm),
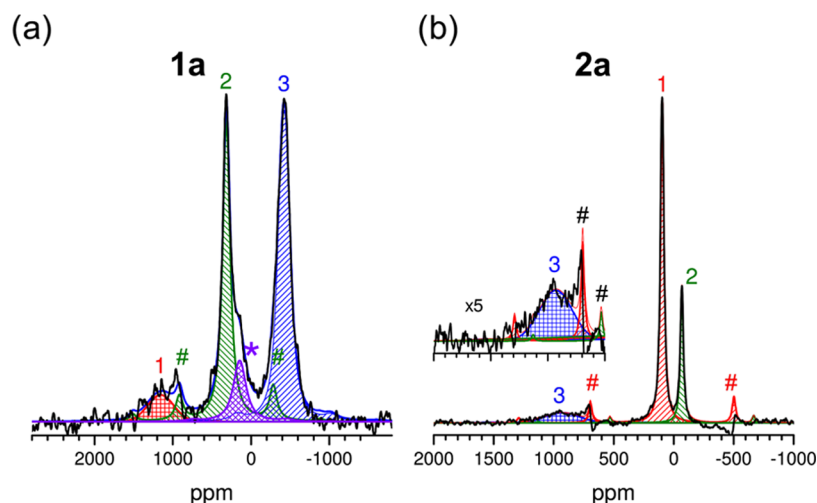
Figure 2. ^{13}C MAS NMR spectra of compounds (a) **1a** and (b) **2a** obtained in the solid state (30 kHz spinning) at 313 K. The NMR lines assigned to atoms C1, C2, and C3 are colored in red, green, and blue, respectively. The hash marks (#) denote spinning sidebands, which are out of phase due to the mismatch of the echo delay and the rotation period. The asterisk (*) denotes an additional signal in the sample of **1a**. The NMR spectra (average of 10^5–10^6 scans) were recorded by a spin-echo pulse sequence with a short delay (10 μs) between the excitation and refocusing pulses and a relaxation delay of 25 ms. For more experimental details, see Section 4 and the Supporting Information (Table S1, Figures S1 and S2).

Table 1. Experimental ^1H (Solution, $CDCl_3$) and ^{13}C (Solid State) NMR Shifts for Compounds 1a−d and 2a−d Measured at 313 K

compound	atom	^1H (solution)	^{13}C (solid state)
1a	C1		+1155
(R = H)	H2/C2	+26.9	+316
	H3/C3	+38.1	−421
1b	C1		a
(R = CN)	C2		a
	H3/C3	+44.4	−340
1c	C1		a
(R = Cl)	C2		a
	H3/C3	+38.9	−250
1d	C1		a
(R = Br)	C2		a
	H3/C3	+38.1	−320
2a	C1		+96
(R = H)	H2/C2	−20.1	−67
	H3/C3	+0.9	+929
2b	C1		+96
(R = CN)	C2		−87
	H3/C3	+2.4[b]	+750
2c	C1		+123
(R = Cl)	C2		−143
	H3/C3	+6.2	+800
2d	C1		+162
(R = Br)	C2		−160
	H3/C3	+7.0	+804

^{a}Not observed. ^{b}Measured in methanol-d_4.

whereas the methyl C3 is notably shielded (δ = −421 ppm). The signal assignment pattern is reversed for **2a**: C1 is slightly shielded compared to its diamagnetic counterparts, but C3 is greatly deshielded (δ = +929 ppm). The experimental (solid state) and DFT-calculated (in vacuo) ^{13}C NMR shifts of atoms C1−C3 in compounds **1a** and **2a** are shown in Figure 3.

The NMR shifts for compounds **1** reported in this work have been calculated assuming a quartet ground state, eq 2. This is perfectly justified by the vanishingly small experimental ZFS (D < 0.6 cm^{-1} for **1a**)[28,29] and our comparison between the NMR shifts calculated with and without ZFS (Table S2). To determine the physical contributions to the hyperfine NMR shifts that dominate the trends in Figure 3, we performed

theoretical calculations of the hyperfine coupling tensors at the four-component relativistic DFT level (Table S3 in the Supporting Information).[30] The values obtained for the isolated molecules are summarized in Table S4 and confirm the dominant role of the Fermi-contact contributions related to the distribution of electron-spin density in the β-diketonato moiety, which will be discussed in detail in Section 2.3. Note that the NMR shifts for **2a** calculated in vacuo (Figure 3) agree nicely with those reported previously (+1153, +149, and −44 ppm).[21]

The successful observation of all of the ^{13}C NMR resonances of parent compounds **1a** and **2a** (including those at around 1000 ppm) prompted us to investigate the set of compounds **1** and **2** shown in Figure 1 and to analyze the effects of substituents on the NMR shifts. However, for the chromium complexes **1**, we obtained the NMR resonances of C1 (+1155 ppm) and C2 (+316 ppm) only for compound **1a**. Our inability to detect NMR signals of these two atoms for the other Cr(III) complexes can be rationalized by either the presence of several molecules in the asymmetric unit of our crystalline samples or very fast transverse relaxation or both. However, as the trends in NMR shifts for **1a** and **2a** are satisfactorily reproduced by theoretical calculations (see Figure 3), we visualize the theoretical substituent-dependent ^{13}C NMR shift of C2 in Figure 4. Substituting bromine for hydrogen in compound **1** results in an additional deshielding of C2 by almost 700 ppm (compare δ_{C2}^{tot} for **1a** and **1d** in Figure 4), accounted for mainly by the contribution of the hyperfine shift. The electronic origins of the individual hyperfine contributions will be discussed in detail in Sections 2.3 and 2.4.

2.2. DFT Calculation of NMR Shifts at Experimental Conditions. Despite the general agreement of the trends in the NMR shifts shown in Figures 3 and 4, there is a significant mismatch between the experimental solid-state data and the theoretical values calculated in vacuo, as shown in Table 2 and Figure 5. We therefore investigated the individual physical effects influencing the NMR shifts. Because of the planar nature of the Cu(II) compounds and their assumed greater sensitivity to intermolecular contacts including cation−π interactions, compound **2a** is analyzed in this section as an example.

2.2.1. Crystal Packing. First, we investigated the effect of crystal packing on the NMR shift using the cluster
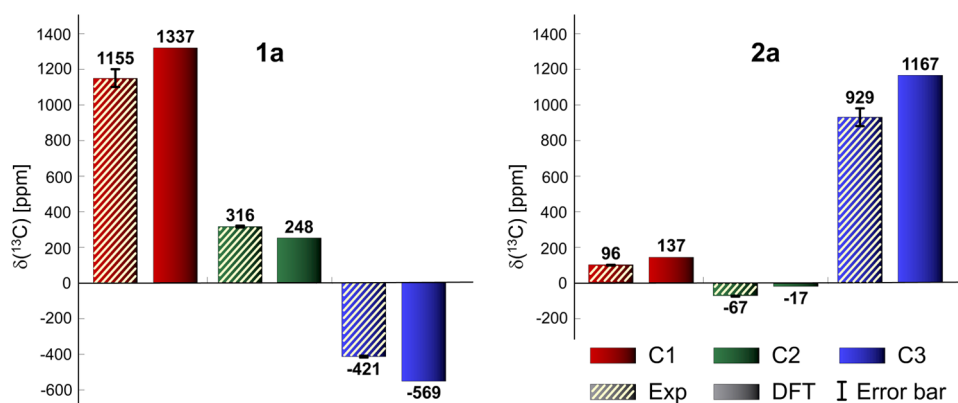
Figure 3. Experimental (solid state, stripe pattern) and theoretical (DFT-calculated in vacuo using ADF2017, see Section 4) ^{13}C NMR shifts of atoms C1 (red), C2 (green), and C3 (blue) in compounds **1a** (left) and **2a** (right) at 313 K. The estimated uncertainty of the experimental NMR shifts is shown by standard error bars.
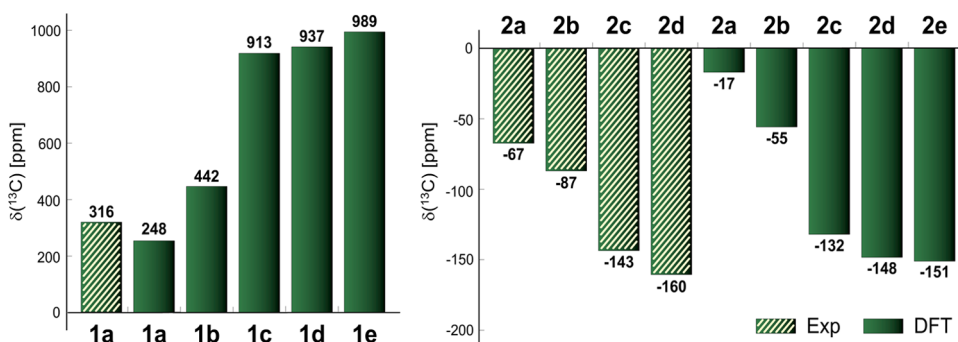
Figure 4. Experimental (solid state) and theoretical (DFT-calculated in vacuo using ADF2017) ^{13}C NMR shifts of C2 for compounds **1a−1e** (left) and **2a−2e** (right) at 313 K.

Table 2. NMR Shifts for Compounds 1a ($S = 3/2$) and 2a ($S = 1/2$) Calculated Using PBE0/TZ2P In Vacuo or in a Supramolecular Cluster^c

	atom	vacuo^a	vacuo^b	clust(3)	clust(3$^{\uparrow\downarrow}$)^d	$\Delta^{\uparrow\downarrow}$	clust(9)	clust(9) + $\Delta^{\uparrow\downarrow}$	**exp**
1a	C1	+1337	+1304	+1291			+1286		**+1155**
	C2	+248	+254	+268			+266		**+316**
	C3	−569	−567	−551			−531		**−421**
2a	C1	+137	+107	+86	+86	+0	+83	+83	**+96**
	C2	−17	−25	−32	−57	−25	−39	−64	**−67**
	C3	+1167	+1168	+1092	+988	−104	+1059	+955	**+929**

^{c}The geometry of the central molecule was optimized in the supramolecular cluster unless stated otherwise; see Section 4. ^{a}Geometry optimized in vacuo (EPR and NMR parameters calculated in vacuo using ADF2017). ^{b}Geometry optimized in clust(9) (EPR and NMR parameters calculated in vacuo using ADF2019 and ADF2017, respectively); clust(3): two cluster neighbors are diamagnetic (with Ca atoms). ^{d}clust(3$^{\uparrow\downarrow}$): all three molecules are open shell (see Table 3); $\Delta^{\uparrow\downarrow}$: calculated as clust(3$^{\uparrow\downarrow}$) − clust(3); clust(9): eight cluster neighbors are diamagnetic (with Ga and Ca atoms for **1a** and **2a**, respectively); for Cartesian coordinates, see the Supporting Information; exp: experimental solid-state NMR data.
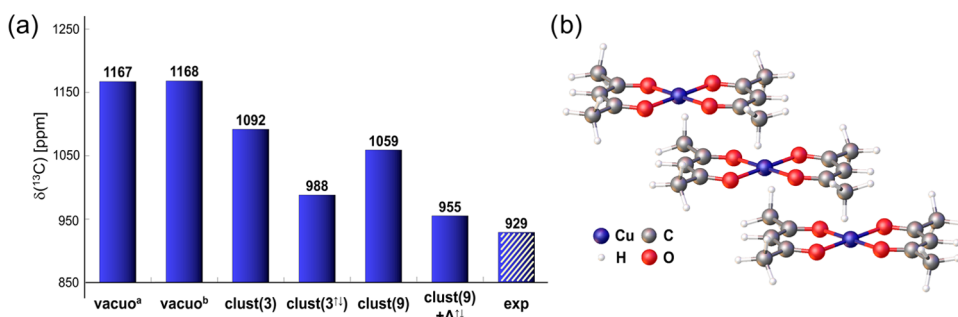
Figure 5. (a) Contributions of individual physical effects to the NMR shift of C3 in compound **2a** as described in Table 2. (b) Side view of the supramolecular arrangement of two nearest-neighbor molecules in the small cluster (clust-3) of compound **2a** indicating intermolecular cation−π interaction between Cu and C2 (plotted by the OLEX2 program^{31}).

approach.$^{32−34}$ The central molecule of interest was embedded in a cluster of eight surrounding molecules generated from the X-ray structure ACACCU04^{35} ($R = 2.2$), clust(9). Calcium atoms were substituted for copper in all of the embedding diamagnetic molecules (for the cluster arrangement, see Cartesian coordinates in the Supporting Information). The NMR shift of C3 in the central molecule of **2a** in this large clust(9) changed by 109 ppm, as shown in Table 2 and Figure 5. However, approximately 70% of this supramolecular effect on the C3 NMR shifts for **2a** had already been reproduced by the two nearest neighbors in clust(3). Therefore, we analyze only the small clust(3) of **2a** in the following section.

2.2.2. Effect of Neighboring Paramagnetic Molecules. To investigate the hyperfine effects of paramagnetic neighbors on the NMR shifts of the central molecule of **2a** in the solid state,^{36,37} we resorted to the smallest cluster, the three molecules shown in Figure 5b. Because the magnetic coupling

constant and zero-field splitting are negligible, the electronic ground state of this clust(3$^{\uparrow\downarrow}$) is eight-times degenerate (one quartet and two doublets). This degeneracy permits us to use eight single Slater determinants (Ψ^{SD}) to describe its electronic states. To choose unique Ψ^{SD} (with different NMR values), we fix the α electron-spin state at the central probing molecule (labeled as a bold ↑). As a result, four spin combinations at the two neighboring paramagnetic centers are possible, one Ψ^{SD} with three unpaired spins (↑↑↑) and three Ψ^{SD} with one unpaired spin (↓↑↑, ↑↑↓, and ↓↑↓). The EPR and NMR parameters calculated for the individual spin systems using the ZORA approach are summarized in Table 3. Clearly, the differences between the ^{13}C NMR shifts calculated for the individual ↓↑↑, ↑↑↓, and ↓↑↓ states are rather marginal (<15 ppm). However, the NMR values for the ↑↑↑ state are notably different. Its 25% contribution to clust(3$^{\uparrow\downarrow}$) brings the theoretical values significantly closer to the experiment. The

Table 3. Theoretical Boltzmann Populations (in %) and ^{13}C NMR Shifts (in ppm), Calculated Using the ZORA Approach and the PBE0 Functional, for the Individual Spin States of clust($3^{\uparrow\downarrow}$) and the Averaged Values[a]

	↑↑↑	↓↑↑	↑↑↓	↓↑↓	clust($3^{\uparrow\downarrow}$)
population	25	25	25	25	
C1	+18	+104	+105	+118	+86
C2	−192	−27	−28	−22	−57
C3	+1367	+857	+861	+868	+988

[a]For computational details, see Section 4.

averaged ^{13}C NMR shifts are included in Table 2 to calculate the shielding correction ($\Delta^{\uparrow\downarrow}$) used further for the calculation on the large clust(9). Summing up all of the physical effects in Table 2 results in very satisfactory agreement between the theoretical and experimental ^{13}C NMR data for **2a** ($\Delta\delta < 30$ ppm).

2.2.3. Comment on the Selection of the Density Functional. The calculation of NMR and EPR parameters has previously been shown to be very sensitive to the density functional, particularly the amount of the exact-exchange admixture used.[5,24,38] The effect of the exact-exchange admixture (0−40%) in the PBE-based functional for compounds **1a** and **2a** is shown in Table S8 and Figure S3 (Supporting Information). This effect amounts to up to 500 ppm (C1) and 800 ppm (C3) for compounds **1a** and **2a**, respectively. However, the use of a reliable structural model and the simulation of crystal packing by the cluster approach provide very good agreement between the theoretical and experimental NMR data (Table 2). Therefore, we used 25% of the exact-exchange admixture as implemented in the standard PBE0 functional for all of our production calculations. To interpret the differences in the NMR shifts between compounds **1** and **2**, we first analyze and discuss their electronic structures.

2.3. Differences between Compounds 1a (d^3) and 2a (d^9). *2.3.1. Electronic Structure.* Compound **1a** contains three 3d electrons, each occupying a metal-centered d$_{xy}$-, d$_{xz}$-, or d$_{yz}$-based molecular spin orbital (MSO, $S = 3/2$), as shown schematically in Figure 6a. These single-occupied orbitals are of π-symmetry relative to the six Cr−O bonds. Because of the π-symmetry, the spin polarization in π-space is expected to be the main mechanism resulting in a Fermi-contact contribution to the ligand hyperfine ^{13}C NMR shifts of **1a**. However, an additional donation of α-spin density (Hund's rule) to the formally vacant d$_{x^2-y^2}$ and d$_{z^2}$ would result in an overabundance of β-spin density in the ligand σ-space (see below).

In contrast, **2a** has nine 3d electrons. The metal-centered nonbonding molecular spin orbitals (MSOs) of d$_{xy}$-, d$_{xz}$-, d$_{yz}$-, and d$_{z^2}$-type are approximately paired, whereas a single unpaired electron ($S = 1/2$) resides in d$_{x^2-y^2}$; see Figure 6b. The unpaired density is thus found in the σ-space of all of the four Cu−O bonds. Therefore, the σ-bond spin delocalization and hyperconjugation interactions[39] are expected to dominate the Fermi-contact mechanism of the ligand hyperfine ^{13}C NMR shifts in **2a**. The total spin densities for compounds **1a** and **2a**, calculated at the scalar-relativistic (**1c**) level of theory, are visualized in Figure 7.
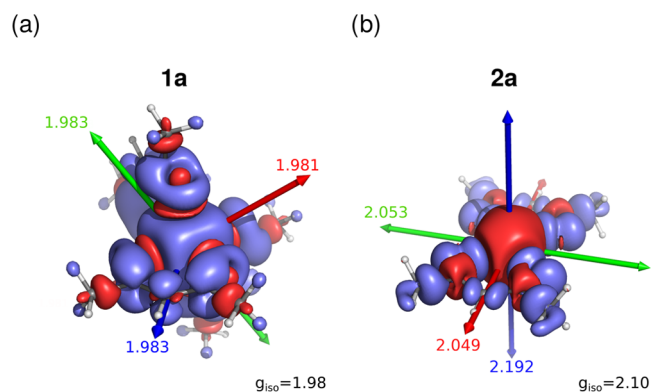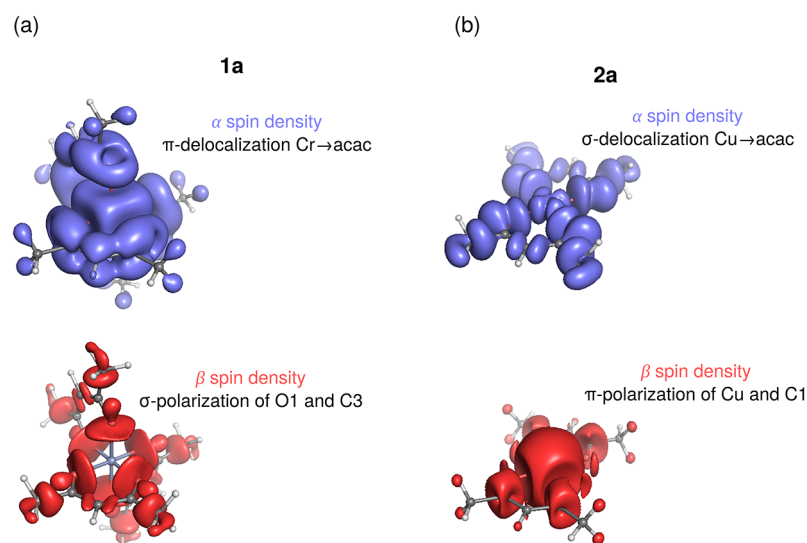

Figure 7. Visualization of the scalar-relativistic (**1c**) spin density (isosurface at ± 0.0002 au) and the principal components of the **g**-tensor for (a) **1a** and (b) **2a**, calculated using DFT at the spin−orbit (**2c**) level; see Section 4. The predominance of the α and β spin density is shown in blue and red, respectively.

As shown in Figure 7, the isotropic g factors (g_{iso}) are opposite for the compounds **1a** and **2a**. Note in passing that our calculated g_{iso} values of 1.98 (**1a**) and 2.10 (**2a**) are in very good agreement with the experimental data reported previously (1.98 for **1a**,[28] 2.12 for **2a**[40]). The signs of the g-shifts (Δg_{iso}) have been interpreted in terms of the electronic structure since the dawn of EPR spectroscopy.[19,41] The angular magnetic couplings in the α-spin space involving a singly occupied molecular orbital (SOMO) result in negative g-shifts (Δg_{iso}) for early TM complexes (d^1−d^3).[18,19] This applies to the d^3 compound **1a** ($\Delta g_{iso} = -20$ ppt), where three singly occupied 3d α orbitals can form efficient angular magnetic couplings with two unoccupied 3d α orbitals, whereas three singly unoccupied 3d β orbitals have no occupied β d-orbitals nearby with which to form efficient magnetic couplings (see Figure 6). In contrast, couplings in the β-spin space involving singly unoccupied molecular orbital (SUMO) result in positive
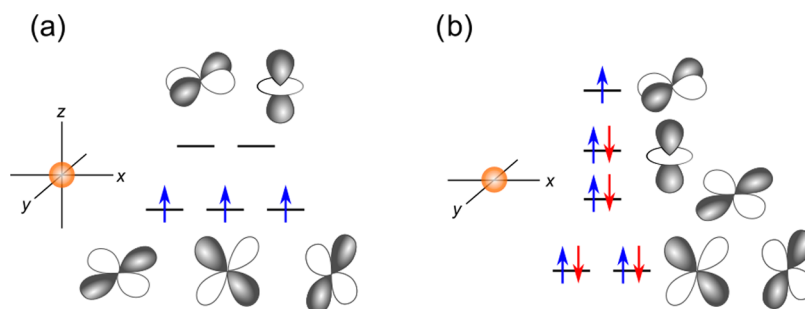
Figure 6. Schematic representation of the energy and occupation of metal 3d orbitals in compounds (a) **1a** and (b) **2a**. Note that the ligands occupy x, y, z and x, y positions in the octahedral and square-planar complexes, respectively.

(a)

1a

α spin density
σ-delocalization Cr→acac

β spin density
σ-polarization of O1 and C3

(b)

2a

α spin density
σ-delocalization Cu→acac

β spin density
π-polarization of Cu and C1

Figure 8. Visualization of the spin density (isosurface at ± 0.0001 au) for compounds (a) **1a** and (b) **2a**, separated into the *α* (top) and *β* (bottom) parts.

g-shifts for the late TM complexes (d^6–d^9).[18,19] This clearly applies to the d^9 compound **2a** (Δg_{iso} = +96 ppt) because several occupied 3d *β* orbitals are available for the *β* SUMO to form angular magnetic couplings, whereas no unoccupied *α* orbitals are accessible to the *α* SOMO (see Figure 6). This has been shown to be the case for 3d TM complexes with acetylacetonate involving V, Ni, and Cu.[21]

2.3.2. Spin Delocalization and Polarization. To analyze the hyperfine coupling pathways for the individual atoms C1–C3 in compounds **1a** and **2a** in detail, the spin densities are plotted separately for *α* and *β* spaces in Figure 8.

In compound **1a**, the spin-propagation mechanism involves two distinct pathways. First, the spin polarization of the σ_{Cr-O} bond, linked with the donation of *α*-spin density (Hund's rule) to the vacant $d_{x^2-y^2}$ and d_{z^2} orbitals, as shown in Figure 6a, leaves *β*-spin density in the σ-space of the ligand, particularly at the oxygen atom (spin population −0.020 au). This polarization is partially transferred to the C3 atom by the Cr−O ↔ C1−C3 σ-hyperconjugation mechanism, giving rise to a negative spin population at C3 (−0.004 au) and a negative hyperfine ^{13}C NMR shift (−421 ppm); see Figure 8a (bottom). Second, conjugation of the π-type single-occupied metal-based d-orbital(s) with the ligand π-type orbitals enables the out-of-plane spin-delocalization mechanism (Figure 8a, top), resulting in positive spin populations (predominance of *α*) in the π-space of C1 (+0.016 au) and C2 (+0.007 au) and positive hyperfine shifts for these carbon atoms. This observation is in agreement with the previously reported data for a series of Cr(III)[42] and Ru(III)[24] *β*-diketonates, which indicated considerable π-type delocalization of the metal electrons through the π* orbitals of the ligands.

Because of the different symmetry of the SOMO ($d_{x^2-y^2}$ in Figure 6b) in compound **2a**, the *α*-delocalization on the σ_{Cu-O} bond results in positive spin density at the oxygen atom (+0.077 au); see Figure 8b. Further, this *α*-delocalization is very efficiently transferred to C3 by the Cu−O ↔ C1−C3 hyperconjugation in σ-space, resulting in a $\delta_{C3}^{HF} > 1000$ ppm. In passing, note the expected absence of a π-mechanism for the C3 atom in both compounds. However, in contrast to that in **1a**, C1 is polarized more indirectly in the π-space of **2a**,

therefore, in the opposite way and notably less efficiently (−0.005 au). Similarly, the in-plane spin imbalance at C2 is relatively weak and probably results from the interplay of two mechanisms: (i) σ-hyperconjugation Cu−O ↔ C1−C2 interaction and (ii) π-polarization by two neighboring C1 atoms.

The in-plane spin densities highlighting inverted spin-polarization patterns on the O−C1−C2−H2 coupling pathway for compounds **1a** and **2a** are shown in Figure 9. Note the

(a)

H2
$\rho^{\alpha-\beta}$ +0.0004 au
δ^{HF} 34.7 ppm

1a

(b)

H2
$\rho^{\alpha-\beta}$ -0.0004 au
δ^{HF} -26.9 ppm

2a
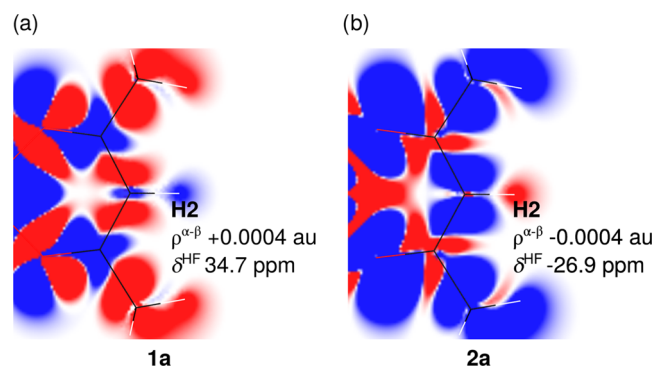
Figure 9. Visualization of the in-plane spin density in the acac ligand for compounds (a) **1a** and (b) **2a**, highlighting the inverted spin-density patterns of the hyperfine coupling pathways toward the C2 and H2 atoms. The atomic spin populations and hyperfine ^{1}H NMR shifts for H2 are included. The predominance of *α* and *β* spin density is shown in blue and red, respectively.

completely opposite patterns at the C1−C2 bond and around C2, which is propagated to the opposite spin polarization at the H2 atom. This is reflected in the positive and negative δ_{H2}^{HF} values for **1a** and **2a**, respectively. The theoretical hyperfine NMR shifts (calculated in vacuo) of +34.7 ppm (**1a**) and −26.9 ppm (**2a**) correspond nicely to the total experimental values (measured in a CDCl$_3$ solution) of +26.9 and −20.1 ppm, respectively, Table 1. Clearly, the opposite patterns of the spin densities in the acac ligands result from the opposite situations at the central metal atoms and the different mechanisms of spin propagation. All of the observations

discussed above are even more pronounced in compounds bearing a polarizable halogen substituent at the C2 atom, as analyzed in detail for the bromo compounds **1d** and **2d** in the following section.

2.4. Substituent Effects on the Spin Densities and Hyperfine NMR Shifts. The Fermi-contact contribution, which dominates the hyperfine ^{13}C NMR shifts discussed in the previous sections, is analyzed here for **1a** vs **1d** and **2a** vs **2d** to reveal the electronic nature of the substituent-induced NMR shifts observed (see Figure 4).

As discussed in Section 2.3, the spin delocalization to C2 in compound **1a** via π-space results in a hyperfine ^{13}C NMR shift of +136 ppm. The presence of a bromine atom at C2 in compound **1d** provides more efficient spin polarization, resulting in δ_{C2}^{HF} = +829 ppm. The difference of almost +700 ppm between these two compounds results from repolarization in the p-orbitals and additional α-spin polarization of the s-orbitals in the bromine compound, as shown by the spatial distribution of the spin density and the differences in the orbital spin populations between **1d** and **1a** in Figure 10a.
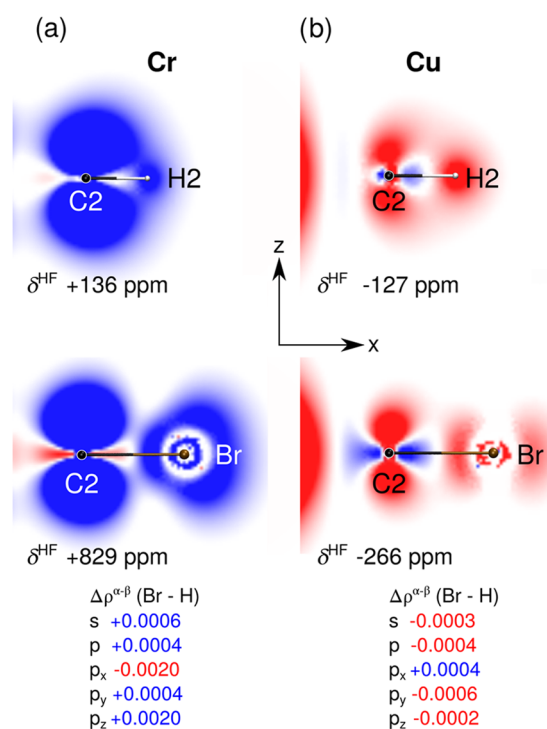
Figure 10. Visualization of the out-of-plane spin density on the C2−X bond for compounds (a) **1a** (X = H) and **1d** (X = Br) and (b) **2a** (X = H) and **2d** (X = Br). The differences in the spin populations of the AOs between derivatives **a** (top) and **d** (bottom) are also presented.

Similarly, the more negative hyperfine ^{13}C NMR shift of C2 for **2d** as compared with that for **2a** reflects an increased imbalance in the spin distribution around the C2 nucleus favoring β-spin density; see Figure 10b.

The observations and differences in spin distribution summarized above result from the different electronegativities of the X atom (H vs Br) at C2, the polarizabilities of the C2−X bonds, and the related different degrees of hybridization at C2. The more polarizable and longer C2−Br bond involves more carbon 2p-character, leaving the carbon 2s orbital less affected and more symmetrically distributed at all three bonds around C2 and, therefore, available for symmetrical polarization

around the carbon nucleus; see Figure 10, bottom. In general, this rearrangement results in a significantly larger Fermi-contact contribution to the hyperfine NMR shifts for the **d** compounds. Similar arguments apply to the other derivatives with halogens, compounds **c** and **e** (cf., Figure 4). A detailed investigation of the effects of substituents on the spin-polarization and hyperfine coupling pathways in a large set of transition-metal complexes is in progress in our laboratories.

3. CONCLUSIONS

Carefully measured, calculated, and interpreted ligand NMR data for two series of paramagnetic acetylacetonate complexes are reported. For the first time, solid-state ^{13}C NMR resonances for greatly paramagnetically deshielded carbon atoms in Cr(III) and Cu(II) compounds were obtained by a short spin-echo MAS experiment. The trends in experimental NMR shifts have been reproduced by the DFT calculations for isolated molecules. However, quantitative agreement between the experimental solid-state and theoretical DFT values is shown to be achieved only if the effects of the supramolecular interactions in the crystal and nearest-neighbor paramagnetic molecules are included. Our contribution provides a guide for many future NMR investigations of complex systems.

The differences in ^{13}C NMR resonances between octahedral d^3 Cr(acac)$_3$ and square-planar d^9 Cu(acac)$_2$ compounds are rationalized by the molecular symmetry, the electronic and spin structure, and different spin-delocalization mechanisms involving conjugation in π-space and hyperconjugation in σ-space. Further, the substituent-induced hyperfine effects are shown to amount up to 700 ppm, calculated as a difference between the ^{13}C shifts of C2 in compounds with the hydrogen (**a**) and bromine (**d**) atom. However, a full understanding of this substituent-induced effect requires that additional analyses be performed and it cannot be rationalized by simply plotting the spin densities and total atomic spin populations. The analysis of hyperfine coupling pathways in a heavy-element series of acetylacetonates using hyperfine coupling densities is in progress in our laboratories.

4. EXPERIMENTAL AND THEORETICAL METHODS

4.1. Materials and Synthesis. The starting compounds CrCl$_3$· xH$_2$O, CuCl$_2$·xH$_2$O, 2,4-pentanedione, N-bromosuccinimide, NaHCO$_3$, K$_2$CO$_3$, Cu(NO$_3$)$_2$·3H$_2$O, acetic anhydride, and CH$_3$COONa were used as obtained from our suppliers. The solvents in p.a. grade were used as received without further purification. The compounds were synthesized according to slightly modified procedures reported previously, as described in the Supporting Information.

4.2. NMR Spectroscopy. *4.2.1. Solid-State NMR.* ^1H and ^{13}C MAS NMR spectra of compounds **1** and **2** were recorded on a Bruker AVANCE-II spectrometer at a magnetic field of 4.7 T (200.06 and 50.31 MHz for ^1H and ^{13}C, respectively) using a home-built MAS probe for 1.8 mm Si$_3$N$_4$ rotors. The NMR shifts are given using a TMS scale. The temperature of a spinning sample depends on the spinning speed and on the air flow in the driving and bearing channels. The actual temperature of the sample has been calibrated using the NMR shift of lead nitrate, Pb(NO$_3$)$_2$, which was spun under identical conditions.[43]

The ^1H MAS spectra were recorded with the spin-echo pulse sequence $\pi/2-\tau-\pi-\tau-$ACQ, where $\pi/2$ = 1.5 μs. The sample spinning rate was 40 kHz, and the echo delay was set to one sample rotation period $\tau = \tau_r$ = 25 μs. The spectra were recorded from 1 to 2 × 10^3 repetitions and with a 100−200 ms of relaxation delay.

The ^{13}C MAS spectra were also recorded with a spin-echo pulse sequence ($\pi/2$ = 2.5 μs), but a minimal echo delay of 7−10 μs was

used to minimize the signal decay of the broad NMR lines with the short relaxation times. A spin-echo mismatch caused the spinning sidebands to appear out of phase; see Figure 2. The sample spinning rate was 30 kHz, and the spectra were recorded from 0.1 to 2.5×10^6 repetitions with a 100−200 ms relaxation delay.

4.2.2. NMR in Solution. The ^1H NMR spectra of compounds **1** and **2** were recorded on Bruker AVANCE NEO spectrometers at frequencies of 500 and 700 MHz. The NMR shifts are reported relative to TMS, the reference used. The temperature of the NMR sample was calibrated as reported previously.[24]

4.3. Quantum Chemical Calculations. *4.3.1. Geometry of the Isolated Molecules.* The molecular geometries of compounds **1** and **2** were fully optimized in vacuo using the PBE0 functional[44,45] and the def2-TZVPP basis set (with the corresponding def2-ECP for heavier atoms)[46] as implemented in the Turbomole 7.00 program.[47] All calculations using this optimized protocol[48,49] were performed with the m5 integration grid and the following convergence criteria: 10^{-6} for the energy change and 10^{-3} for the geometry gradient.

4.3.2. Geometry in the Solid State. The starting structures for compounds **1a** and **2a** were extracted from the X-ray data with reference codes ACACCR07 ($R = 4.2$)[50] and ACACCU04 ($R = 2.2$),[35] respectively. The central molecule of interest was embedded in a cluster of eight surrounding diamagnetic molecules (Ga and Ca were substituted for Cr and Cu, respectively) generated from the crystal packing. We used an approach calibrated in our previous studies of octahedral and square-planar transition-metal complexes to optimize the molecular geometry of the central molecule.[5,48] The surrounding cluster was kept fixed (for **1a**) except the positions of all of the hydrogen atoms (for **2a**) that were relaxed (for Cartesian coordinates, see the Supporting Information). The geometry was optimized using density-functional theory (DFT) with the PBE0 functional[44,45] and the def2-TZVPP basis set[46] for all atoms of the central molecule and the def2-SVP basis set for all atoms of the surrounding cluster, with the corresponding relativistic effective core potentials (def2-ECPs)[51] for the metal center. The dispersion correction D3-BJ[52,53] was employed to treat weak supramolecular interactions in the cluster.

4.3.3. Two-Component Calculation of the NMR and EPR Parameters. The total NMR shifts were calculated as the sum of the orbital (δ_L^{orb}) and hyperfine (δ_L^{HF}) contributions, according to eq 1. The orbital shift of the ligand atom L is obtained theoretically as the difference between the shielding constants of a reference diamagnetic compound (σ_{ref}) and a spectator atom L (δ_L^{orb})

$$\delta_L^{orb} = \sigma_{ref} - \sigma_L^{orb} + \delta_{ref} \tag{4}$$

The NMR and EPR parameters were calculated using the zeroth-order regular approximation (ZORA)[54,55] Hamiltonian, as implemented in the ADF program package (versions 2017 and 2019).[56−58] The orbital NMR shielding constants and zero-field splittings for open-shell systems were determined only at the scalar (spin-free, 1c) ZORA level. In the production calculations, we used the PBE0 functional (for other functionals, see the Supporting Information), the TZ2P basis sets,[59] and either vacuum or the cluster model derived from the X-ray geometry (see above). The calculated orbital shifts (δ_L^{orb}) were referenced relative to adamantane as a secondary reference $(\delta_{ref} = 1.82$ ppm for ^1H and $\delta_{ref} = 38.48$ ppm for $^{13}C)$ and are reported relative to TMS (primary reference). The hyperfine shifts (δ_L^{HF}) were calculated at the 2c (SO-ZORA) level using the same functional and basis sets as used for the calculation of the orbital contributions. The zero-field splitting (ZFS) parameters D and E were included in the testing calculations using the pNMRShift program.[60,61] For details and the effects of ZFS on the calculated hyperfine NMR shifts, see the Supporting Information. The reported values were obtained by averaging the corresponding values for all chemically equivalent atoms. The net atomic and orbital spin populations were calculated at the 1c level of theory in the ADF program (ZORA/PBE0) using the Mulliken approach[62] consistent with our previous reports on paramagnetic Ru(III) compounds.[5,24]

4.3.4. Four-Component Calculation of the Fermi-Contact, Spin-Dipolar, and Paramagnetic Spin−Orbit Contributions to the

Hyperfine NMR Shift. The separation of δ_L^{HF} into individual physical terms according to eq 3 was performed as described previously[16,63] at the four-component level of theory employing the ReSpect program package.[30]

■ ASSOCIATED CONTENT

ⓢ Supporting Information

The Supporting Information is available free of charge at https://pubs.acs.org/doi/10.1021/acs.inorgchem.1c00204.

Solid-state NMR spectroscopy, DFT calculations, synthesis, and cartesian coordinates (PDF)

■ AUTHOR INFORMATION

Corresponding Author

Radek Marek − *CEITEC—Central European Institute of Technology, Masaryk University, CZ-625 00 Brno, Czechia; Department of Chemistry, Faculty of Science and National Center for Biomolecular Research, Faculty of Science, Masaryk University, CZ-625 00 Brno, Czechia;* ⓞ orcid.org/0000-0002-3668-3523; Email: radek.marek@ceitec.muni.cz

Authors

Jan Novotný − *CEITEC—Central European Institute of Technology, Masaryk University, CZ-625 00 Brno, Czechia; Department of Chemistry, Faculty of Science, Masaryk University, CZ-625 00 Brno, Czechia; Institute of Inorganic Chemistry, Slovak Academy of Sciences, SK-84536 Bratislava, Slovakia;* ⓞ orcid.org/0000-0002-1203-9549

Lukáš Jeremias − *CEITEC—Central European Institute of Technology, Masaryk University, CZ-625 00 Brno, Czechia; Department of Chemistry, Faculty of Science, Masaryk University, CZ-625 00 Brno, Czechia; Department of Chemistry and Biochemistry, Faculty of AgriSciences, Mendel University, CZ-613 00 Brno, Czechia;* ⓞ orcid.org/0000-0001-8744-6897

Patrick Nimax − *CEITEC—Central European Institute of Technology, Masaryk University, CZ-625 00 Brno, Czechia; National Center for Biomolecular Research, Faculty of Science, Masaryk University, CZ-625 00 Brno, Czechia*

Stanislav Komorovsky − *Institute of Inorganic Chemistry, Slovak Academy of Sciences, SK-84536 Bratislava, Slovakia;* ⓞ orcid.org/0000-0002-5317-7200

Ivo Heinmaa − *National Institute of Chemical Physics and Biophysics, EE-12618 Tallinn, Estonia*

Complete contact information is available at:
https://pubs.acs.org/10.1021/acs.inorgchem.1c00204

Author Contributions

[∇]J.N. and L.J. contributed equally to this work.

Notes

The authors declare no competing financial interest.

■ ACKNOWLEDGMENTS

■ REFERENCES

(1) La Mar, G. N.; DeW Horrocks, W.; Holm, R. H. *NMR of Paramagnetic Molecules*; Academic Press: New York, 1973.

(2) Bertini, I.; Luchinat, C.; Parigi, G.; Ravera, E. *NMR of Paramagnetic Molecules: Applications to Metallobiomolecules and Models*; Elsevier: Amsterdam, 2016.

(3) Kaupp, M.; Köhler, F. H. Combining NMR Spectroscopy and Quantum Chemistry as Tools to Quantify Spin Density Distributions in Molecular Magnetic Compounds. *Coord. Chem. Rev.* **2009**, *253*, 2376−2386.

(4) Pell, A. J.; Pintacuda, G.; Grey, C. P. Paramagnetic NMR in Solution and the Solid State. *Prog. Nucl. Magn. Reson. Spectrosc.* **2019**, *111*, 1−271.

(5) Novotný, J.; Sojka, M.; Komorovsky, S.; Nečas, M.; Marek, R. Interpreting the Paramagnetic NMR Spectra of Potential Ru(III) Metallodrugs: Synergy between Experiment and Relativistic DFT Calculations. *J. Am. Chem. Soc.* **2016**, *138*, 8432−8445.

(6) Moon, S.; Patchkovskii, S. First-Principles Calculations of Paramagnetic NMR Shifts. In Calculation of NMR and EPR Parameters. In *Theory and Applications*; Kaupp, M.; Bühl, M.; Malkin, V. G., Eds.; Wiley-VCH: Weinheim, 2004; pp 325−328.

(7) Komorovsky, S.; Repisky, M.; Ruud, K.; Malkina, O. L.; Malkin, V. G. Four-Component Relativistic Density Functional Theory Calculations of NMR Shielding Tensors for Paramagnetic Systems. *J. Phys. Chem. A* **2013**, *117*, 14209−14219.

(8) Van den Heuvel, W.; Soncini, A. NMR Chemical Shift in an Electronic State with Arbitrary Degeneracy. *Phys. Rev. Lett.* **2012**, *109*, No. 073001.

(9) Van den Heuvel, W.; Soncini, A. NMR Chemical Shift as Analytical Derivative of the Helmholtz Free Energy. *J. Chem. Phys.* **2013**, *138*, No. 054113.

(10) Hrobárik, P.; Reviakine, R.; Arbuznikov, A. V.; Malkina, O. L.; Malkin, V. G.; Köhler, F. H.; Kaupp, M. Density Functional Calculations of NMR Shielding Tensors for Paramagnetic Systems with Arbitrary Spin Multiplicity: Validation on 3d Metallocenes. *J. Chem. Phys.* **2007**, *126*, No. 024107.

(11) Gendron, F.; Sharkas, K.; Autschbach, J. Calculating NMR Chemical Shifts for Paramagnetic Metal Complexes from First-Principles. *J. Phys. Chem. Lett.* **2015**, *6*, 2183−2188.

(12) Rouf, S. A.; Mareš, J.; Vaara, J. 1H Chemical Shifts in Paramagnetic Co(II) Pyrazolylborate Complexes: A First-Principles Study. *J. Chem. Theory Comput.* **2015**, *11*, 1683−1691.

(13) Vaara, J.; Rouf, S. A.; Mareš, J. Magnetic Couplings in the Chemical Shift of Paramagnetic NMR. *J. Chem. Theory Comput.* **2015**, *11*, 4840−4849.

(14) Vaara, J. Chemical Shift in Paramagnetic Systems. In High Resolution NMR Spectroscopy: Understanding Molecules and Their Electronic Structures. In *Science and Technology of Atomic Molecular Condensed Matter and Biological Systems*; Contreras, R. H.; Contreras, R. H., Eds.; Elsevier, 2013; pp 41−67.

(15) Autschbach, J. NMR Calculations for Paramagnetic Molecules and Metal Complexes. In *Annual Reports in Computational Chemistry*; Dixon, D. A., Ed.; Elsevier, 2015; Chapter 1, Vol. *11*, pp 3−36.

(16) Novotný, J.; Přichystal, D.; Sojka, M.; Komorovsky, S.; Nečas, M.; Marek, R. Hyperfine Effects in Ligand NMR: Paramagnetic Ru(III) Complexes with 3-Substituted Pyridines. *Inorg. Chem.* **2018**, *57*, 641−652.

(17) Chyba, J.; Novák, M.; Munzarová, P.; Novotný, J.; Marek, R. Through-Space Paramagnetic NMR Effects in Host−Guest Com-

plexes: Potential Ruthenium(III) Metallodrugs with Macrocyclic Carriers. *Inorg. Chem.* **2018**, *57*, 8735−8747.

(18) Bora, P. L.; Novotný, J.; Ruud, K.; Komorovsky, S.; Marek, R. Electron-Spin Structure and Metal−Ligand Bonding in Open-Shell Systems from Relativistic EPR and NMR: A Case Study of Square-Planar Iridium Catalysts. *J. Chem. Theory Comput.* **2019**, *15*, 201−214.

(19) Mabbs, F. E.; Collison, D. *Electron Paramagnetic Resonance of d Transition Metal Compounds*; Elsevier Science: Amsterdam, 1992; Vol. *16*, pp 338−441.

(20) Abragam, A.; Bleaney, B. *Electron Paramagnetic Resonance of Transition Ions*; Oxford Classic Texts in the Physical Sciences; Oxford University Press: Oxford, New York, 2012.

(21) Andersen, A. B. A.; Pyykkönen, A.; Jensen, H. J. A.; McKee, V.; Vaara, J.; Nielsen, U. G. Remarkable Reversal of 13C-NMR Assignment in D1, D2 Compared to D8, D9 Acetylacetonate Complexes: Analysis and Explanation Based on Solid-State MAS NMR and Computations. *Phys. Chem. Chem. Phys.* **2020**, *22*, 8048−8059.

(22) Pritchard, B.; Autschbach, J. Theoretical Investigation of Paramagnetic NMR Shifts in Transition Metal Acetylacetonato Complexes: Analysis of Signs, Magnitudes, and the Role of the Covalency of Ligand−Metal Bonding. *Inorg. Chem.* **2012**, *51*, 8340−8351.

(23) Rastrelli, F.; Bagno, A. Predicting the NMR Spectra of Paramagnetic Molecules by DFT: Application to Organic Free Radicals and Transition-Metal Complexes. *Chem. - Eur. J.* **2009**, *15*, 7990−8004.

(24) Jeremias, L.; Novotný, J.; Repisky, M.; Komorovsky, S.; Marek, R. Interplay of Through-Bond Hyperfine and Substituent Effects on the NMR Chemical Shifts in Ru(III) Complexes. *Inorg. Chem.* **2018**, *57*, 8748−8759.

(25) Lennartson, A.; Christensen, L. U.; McKenzie, C. J.; Nielsen, U. G. Solid State 13C and 2H NMR Investigations of Paramagnetic [Ni(II)(Acac)2L2] Complexes. *Inorg. Chem.* **2014**, *53*, 399−408.

(26) Rouf, S. A.; Jakobsen, V. B.; Mareš, J.; Jensen, N. D.; McKenzie, C. J.; Vaara, J.; Nielsen, U. G. Assignment of Solid-State 13C and 1H NMR Spectra of Paramagnetic Ni(II) Acetylacetonate Complexes Aided by First-Principles Computations. *Solid State Nucl. Magn. Reson.* **2017**, *87*, 29−37.

(27) Kaupp, M.; Bühl, M.; Malkin, V. G. *Calculation of NMR and EPR Parameters: Theory and Applications*; Wiley-VCH: Weinheim, 2004.

(28) Singer, L. S. Paramagnetic Resonance Absorption in Some Cr +3 Complexes. *J. Chem. Phys.* **1955**, *23*, 379−388.

(29) Sugisaki, K.; Toyota, K.; Sato, K.; Shiomi, D.; Takui, T. Behaviour of DFT-Based Approaches to the Spin−Orbit Term of Zero-Field Splitting Tensors: A Case Study of Metallocomplexes, M III (Acac) 3 (M = V, Cr, Mn, Fe and Mo). *Phys. Chem. Chem. Phys.* **2017**, *19*, 30128−30138.

(30) Repisky, M.; Komorovsky, S.; Kadek, M.; Konecny, L.; Ekström, U.; Malkin, E.; Kaupp, M.; Ruud, K.; Malkina, O. L.; Malkin, V. G. ReSpect: Relativistic Spectroscopy DFT Program Package. *J. Chem. Phys.* **2020**, *152*, No. 184101.

(31) Dolomanov, O. V.; Bourhis, L. J.; Gildea, R. J.; Howard, J. aK.; Puschmann, H. OLEX2: A Complete Structure Solution, Refinement and Analysis Program. *J. Appl. Crystallogr.* **2009**, *42*, 339−341.

(32) Maliňáková, K.; Novosadová, L.; Lahtinen, M.; Kolehmainen, E.; Brus, J.; Marek, R. 13C Chemical Shift Tensors in Hypoxanthine and 6-Mercaptopurine: Effects of Substitution, Tautomerism, and Intermolecular Interactions. *J. Phys. Chem. A* **2010**, *114*, 1985−1995.

(33) Babinský, M.; Bouzková, K.; Pipíška, M.; Novosadová, L.; Marek, R. Interpretation of Crystal Effects on NMR Chemical Shift Tensors: Electron and Shielding Deformation Densities. *J. Phys. Chem. A* **2013**, *117*, 497−503.

(34) Bouzková, K.; Babinský, M.; Novosadová, L.; Marek, R. Intermolecular Interactions in Crystalline Theobromine as Reflected in Electron Deformation Density and 13 C NMR Chemical Shift Tensors. *J. Chem. Theory Comput.* **2013**, *9*, 2629−2638.

(35) Golchoubian, H. Redetermination of Crystal Structure of Bis(2,4-Pentanedionato)Copper(II). *Asian J. Chem.* **2008**, *20*, 5834−5838.

(36) Bühl, M.; Ashbrook, S. E.; Dawson, D. M.; Doyle, R. A.; Hrobárik, P.; Kaupp, M.; Smellie, I. A. Paramagnetic NMR of Phenolic Oxime Copper Complexes: A Joint Experimental and Density Functional Study. *Chem. - Eur. J.* **2016**, *22*, 15328−15339.

(37) Mali, G.; Mazaj, M. Hyperfine Coupling Constants in Cu-Based Crystalline Compounds: Solid-State NMR Spectroscopy and First-Principles Calculations with Isolated-Cluster and Extended Periodic-Lattice Models. *J. Phys. Chem. C* **2021**, *125*, 4655−4664.

(38) Hrobárik, P.; Repiský, M.; Komorovský, S.; Hrobáriková, V.; Kaupp, M. Assessment of Higher-Order Spin−Orbit Effects on Electronic g-Tensors of D1 Transition-Metal Complexes by Relativistic Two- and Four-Component Methods. *Theor. Chem. Acc.* **2011**, *129*, 715−725.

(39) Martin, B.; Autschbach, J. Kohn-Sham Calculations of NMR Shifts for Paramagnetic 3d Metal Complexes: Protocols, Delocalization Error, and the Curious Amide Proton Shifts of a High-Spin Iron(II) Macrocycle Complex. *Phys. Chem. Chem. Phys.* **2016**, *18*, 21051−21068.

(40) Adato, I.; Eliezer, I. Effect of the Solvent on the ESR Parameters of Copper Acetylacetonate. *J. Chem. Phys.* **1971**, *54*, 1472−1476.

(41) Symons, M. C. R. *Chemical and Biochemical Aspects of Electron Spin Resonance Spectroscopy*; Van Nostrand Reinhold Inc: New York, US, 1978.

(42) Lintvedt, R. L.; Fatta, N. M. Nephelauxetic and Spectrochemical Series for 1,3-Diketonates. Ligand Field Spectra of Some Tris(1,3-Diketonato)Chromium(III) Chelates. *Inorg. Chem.* **1971**, *10*, 478−481.

(43) Guan, X.; Stark, R. E. A General Protocol for Temperature Calibration of MAS NMR Probes at Arbitrary Spinning Speeds. *Solid State Nucl. Magn. Reson.* **2010**, *38*, 74−76.

(44) Adamo, C.; Barone, V. Toward Reliable Density Functional Methods without Adjustable Parameters: The PBE0 Model. *J. Chem. Phys.* **1999**, *110*, 6158−6170.

(45) Adamo, C.; Scuseria, G. E.; Barone, V. Accurate Excitation Energies from Time-Dependent Density Functional Theory: Assessing the PBE0 Model. *J. Chem. Phys.* **1999**, *111*, 2889−2899.

(46) Schäfer, A.; Huber, C.; Ahlrichs, R. Fully Optimized Contracted Gaussian Basis Sets of Triple Zeta Valence Quality for Atoms Li to Kr. *J. Chem. Phys.* **1994**, *100*, 5829−5835.

(47) *TURBOMOLE V7.0 2015*; TURBOMOLE GmbH. http://www.turbomole.com, 2007.

(48) Vícha, J.; Patzschke, M.; Marek, R. A Relativistic DFT Methodology for Calculating the Structures and NMR Chemical Shifts of Octahedral Platinum and Iridium Complexes. *Phys. Chem. Chem. Phys.* **2013**, *15*, 7740−7754.

(49) Vícha, J.; Novotný, J.; Straka, M.; Repisky, M.; Ruud, K.; Komorovsky, S.; Marek, R. Structure, Solvent, and Relativistic Effects on the NMR Chemical Shifts in Square-Planar Transition-Metal Complexes: Assessment of DFT Approaches. *Phys. Chem. Chem. Phys.* **2015**, *17*, 24944−24955.

(50) Chrzanowski, L. S.; von Lutz, M.; Spek, A. L. α-Tris(2,4-Pentanedionato-κ 2 O, O ′)Cobalt(III) at 240, 210, 180, 150 and 110 K. *Acta Crystallogr., Sect. C: Cryst. Struct. Commun.* **2007**, *63*, m283−m288.

(51) Andrae, D.; Häußermann, U.; Dolg, M.; Stoll, H.; Preuß, H. Energy-Adjusted Ab Initio Pseudopotentials for the Second and Third Row Transition Elements. *Theor. Chim. Acta* **1990**, *77*, 123−141.

(52) Grimme, S.; Antony, J.; Ehrlich, S.; Krieg, H. A Consistent and Accurate Ab Initio Parametrization of Density Functional Dispersion Correction (DFT-D) for the 94 Elements H-Pu. *J. Chem. Phys.* **2010**, *132*, No. 154104.

(53) Grimme, S.; Ehrlich, S.; Goerigk, L. Effect of the Damping Function in Dispersion Corrected Density Functional Theory. *J. Comput. Chem.* **2011**, *32*, 1456−1465.

(54) van Lenthe, E.; Snijders, J. G.; Baerends, E. J. The Zero-order Regular Approximation for Relativistic Effects: The Effect of Spin−Orbit Coupling in Closed Shell Molecules. *J. Chem. Phys.* **1996**, *105*, 6505−6516.

(55) Saue, T. Relativistic Hamiltonians for Chemistry: A Primer. *ChemPhysChem* **2011**, *12*, 3077−3094.

(56) te Velde, G.; Bickelhaupt, F. M.; Baerends, E. J.; Fonseca Guerra, C.; van Gisbergen, S. J. A.; Snijders, J. G.; Ziegler, T. Chemistry with ADF. *J. Comput. Chem.* **2001**, *22*, 931−967.

(57) Guerra, C. F.; Snijders, J. G.; Velde, G.; te Baerends, E. J. Towards an Order-N DFT Method. *Theor. Chem. Acc.* **1998**, *99*, 391−403.

(58) Baerends, E. J.; Ziegler, T.; Atkins, A. J.; Autschbach, J.; Baseggio, O.; Bashford, D.; Bérces, A.; Bickelhaupt, F. M.; Bo, C.; Boerrigter, P. M.; Cavallo, L.; Daul, C.; Chong, D. P.; Chulhai, D. V.; Deng, L.; Dickson, R. M.; Dieterich, J. M.; Ellis, D. E.; van Faassen, M.; Fan, L. *ADF2019, SCM, Theoretical Chemistry*; Vrije Universiteit: Amsterdam: The Netherlands, 2019.

(59) Güell, M.; Luis, J. M.; Solà, M.; Swart, M. Importance of the Basis Set for the Spin-State Energetics of Iron Complexes. *J. Phys. Chem. A* **2008**, *112*, 6384−6391.

(60) Autschbach, J.; Patchkovskii, S.; Pritchard, B. Calculation of Hyperfine Tensors and Paramagnetic NMR Shifts Using the Relativistic Zeroth-Order Regular Approximation and Density Functional Theory. *J. Chem. Theory Comput.* **2011**, *7*, 2175−2188.

(61) Martin, B.; Autschbach, J. Temperature Dependence of Contact and Dipolar NMR Chemical Shifts in Paramagnetic Molecules. *J. Chem. Phys.* **2015**, *142*, No. 054108.

(62) Mulliken, R. S. Electronic Population Analysis on LCAO−MO Molecular Wave Functions, I. *J. Chem. Phys.* **1955**, *23*, 1833−1840.

(63) Haase, P. A. B.; Repisky, M.; Komorovsky, S.; Bendix, J.; Sauer, S. P. A. Relativistic DFT Calculations of Hyperfine Coupling Constants in 5d Hexafluorido Complexes: [ReF6]2− and [IrF6]2−. *Chem. - Eur. J.* **2018**, *24*, 5124−5133.